X-ray Velocimetry and Haemodynamic Forces Within a Stenosed Femoral Model at Physiological Flow Rates

R. Aidan Jamison,[1,2] Stephen Dubsky,[1,2] Karen K. W. Siu,[3] Kerry Hourigan,[1,2] and Andreas Fouras[1]

[1]Division of Biological Engineering, Monash University, Victoria 3800, Australia; [2]Department of Mechanical Engineering, Monash University, Victoria 3800, Australia; and [3]School of Physics, Monash University, Victoria 3800, Australia

Associate Editor Konstantinos Konstantopoulos oversaw the review of this article.

Abstract—High resolution *in vivo* velocity measurements within the cardiovascular system are essential for accurate calculation of vessel wall shear stress, a highly influential factor for the progression of arterial disease. Unfortunately, currently available techniques for *in vivo* imaging are unable to provide the temporal resolution required for velocity measurement at physiological flow rates. Advances in technology and improvements in imaging systems are allowing a relatively new technique, X-ray velocimetry, to become a viable tool for such measurements. This study investigates the haemodynamics of pulsatile blood flow in an optically opaque *in vitro* model at physiological flow rates using X-ray velocimetry. The *in vitro* model, an asymmetric stenosis, is designed as a 3:1 femoral artery with the diameter and flow rate replicating vasculature of a mouse. Velocity measurements are obtained over multiple cycles of the periodic flow at high temporal and spatial resolution (1 ms and 29 μm, respectively) allowing accurate measurement of the velocity gradients and calculation of the wall shear stress. This study clearly illustrates the capability of *in vitro* X-ray velocimetry, suggesting it as a possible measurement technique for future *in vivo* vascular wall shear stress measurement.

Keywords—Particle image velocimetry, Synchrotron imaging, Wall shear stress.

INTRODUCTION

Developing our understanding of arterial disease, currently the leading cause of death and morbidity in the developed world, is an essential step in reducing its effect on the world's population. The link between atherosclerosis, one of the most common forms of arterial disease, and fluid dynamics has been known for over half a century,[43] with more recent studies specifically identifying wall shear stress as being a highly influential factor.[5,33] Computer simulations provide a relatively straightforward way to explore the effect of geometry on flow characteristics, such as wall shear stress (WSS). Although computer simulations can predict the fluid dynamics in anatomically realistic *in vitro* models,[3] assumptions are inevitably made in such models. For example, assuming rigid vessel walls and Newtonian flow,[2,32] which may not be sufficiently physiologically realistic, requires that validation with *in vivo* data should be conducted wherever possible.[10,17] Therefore, research using living tissue is essential for determining the effect that haemodynamics, and the resultant stresses, have on the development and progression of arterial disease. The most widely used model for *in vivo* research, mice, have significant similarity to humans, with 99% of mouse genes having a homologue in the human genome.[31] This, combined with the ability to genetically modify mice, creates a powerful tool in the research of human disease; thus, this study is targeted at future murine research.

Atherosclerosis is a progressive and degenerative disease in which plaque forms on the arterial walls, due to a build up of fatty materials. The formation of plaque is associated with the presence of a low WSS region,[6] with the plaque having a small but gradually increasing effect on the haemodynamics of the flow as it develops. As the plaque increases in size, the caliber of the blood vessel can decrease (stenosis), causing an increase in velocity at the stenosed area and a high WSS region. High WSS and turbulence is seen to harm endothelial cells, initiating platelet activation and causing plaque rupture.[29] As a result, clots form, enter the circulation and may occlude smaller arteries downstream, inducing infarction.[39] At present, the methods used to determine the severity of a stenosis are crude, often relying on the growth rate, constriction size, or even the patient's physical symptoms.[45]

Address correspondence to Andreas Fouras, Division of Biological Engineering, Monash University, Victoria 3800, Australia. Electronic mail: andreas.fouras@monash.edu

These methods are too general and neglect the specific geometry of the stenosis, such as the change in stenosis size along the length of the vessel, which is known to be a highly influential factor on WSS. As it is the flow parameters, not the maximum size of the stenosis, that is thought to influence plaque rupture, it is clear that current diagnostic methods could be improved.

A well-established method for experimentally determining the shear stress that a fluid imparts on a wall is to calculate the gradient of the velocity flow field at the wall. The WSS is defined as

$$\text{WSS} = \mu \frac{\partial u}{\partial y}, \tag{1}$$

where μ is the dynamic viscosity, u is the velocity parallel to the wall, and y is the distance from the wall. Unfortunately, due to the two-phase nature of blood (red blood cells and plasma), whole blood acts as a non-Newtonian fluid, meaning that it does not have a constant dynamic viscosity.[38] The dynamic viscosity of whole blood is generally considered to range between 3 and 4×10^{-3} kg m^{-1} s^{-1} with previous investigations using figures within this range.[23,24,49] Furthermore, to calculate accurately the WSS, high resolution velocity measurements are required at the wall;[15] the current study uses $\mu = 3 \times 10^{-3}$ kg m^{-1} s^{-1} (0.03 dyn s cm^{-2}, 3 cP) for WSS calculation.

The two major clinical techniques used for *in vivo* velocity measurements are magnetic resonance imaging (MRI) and ultrasound. However, MRI and ultrasound are unable to obtain accurate wall shear stress measurements in blood vessels, the majority of which are 1–20 mm in diameter, as their near-wall resolutions, 1000–1200 and 250–300 μm, respectively, are insufficient.[37] Higher resolution is possible in ultrasound but at the expense of penetration, which is acceptable for small animals with vessels within this range. Additionally higher resolution is possible for small animal MRI systems,[4] however, higher resolution is generally gained by a reduction in temporal resolution. High temporal resolution is necessary for *in vivo* studies due to the rapid and highly pulsatile cardiac cycle. A recent study has performed 3D flow reconstruction using ultrasound particle image velocimetry,[35] however, the spatial resolution was an order of magnitude larger than that of the current study.

Particle image velocimetry (PIV)[1] is a laser-based imaging method recognized as one of the most capable techniques for acquiring velocity measurements at the spatial and temporal resolutions required for accurate WSS measurements.[47] However, the opacity of living tissue renders optical-based imaging methods unable to assess internal fluid dynamics, such as in the deep vasculature. Laser-based PIV has previously been conducted *in vivo* for small transparent vessels found in rodents,[41,42] chicken embryos,[25,36,46] and zebrafish embryos.[11,18] Although these studies have provided insight into the development of the heart, investigating minor blood vessels in these animals becomes less relevant to major vessels in human physiology due to the similarity of the vessel diameter and red blood cell (RBC) diameter in the former.

Previous *in vivo* studies using laser-based PIV have either injected tracer particles[41] or, in a novel approach, used the RBCs themselves as the tracer particles.[42] While using RBCs as tracer particles ensures no foreign material is introduced into the blood stream, the RBC depleted region found near vessel walls adversely affects the ability to acquire accurate near wall measurements. Seeding the blood with tracer particles enables measurement of the velocity across the entire vessel, including the RBC depleted region near the vessel wall. This is advantageous for investigating the wall shear stress, which requires high resolution velocity information in the near wall region.

A relatively new technique, X-ray velocimetry,[12,27] allows the investigation of optically opaque specimens, overcoming the restriction of optical access. As an alternative to X-ray absorption imaging, X-ray phase contrast imaging (PCI)[7] utilizes a large propagation distance between the sample and the detector.[13] This distance allows the X-rays after the sample, which are refracted when passing though differing materials, to interfere with the incident X-rays at the detector to produce a characteristic edge enhancement, which serves to also increase contrast and hence signal to noise ratio. Previous work has demonstrated the ability to perform X-ray velocimetry on whole blood without the addition of tracer particles by utilising phase contrast imaging,[19,21,28] but the relatively small phase difference between RBCs and the surrounding tissue renders this technique impractical for *in vivo* studies. Other studies have recently developed bio-compatible microcapsules;[22,26] however, there is yet to be published work using these microcapsules for X-ray velocimetry. Alternatively, commercially available ultrasound contrast agent has been used to seed blood for use in the newly developed technique: computer tomographic X-ray velocimetry (CTXV).[8] Unfortunately, the non-uniform particle size and buoyancy of these contrast agents make them impractical for velocimetry measurements. Additionally, CTXV allows the investigation of highly complex swirling flows.[8,9] However, as the majority of the flow in the vasculature is one-dimensional, a two-dimensional method is used here instead, as its capability to capture instantaneous flow makes it ideal for advancement towards *in vivo* measurements. Furthermore, the current study utilizes

3.5 μm silica microspheres. These particles are available in a range of sizes as small as 0.15 μm and are capable of being coated with a biocompatible surface. Additionally, although the above mentioned X-ray velocimetry work has been successful in measuring blood flows within geometrically realistic *in vitro* models, no study has been capable of conducting such experiments at *in vivo* flow rates. This is the first study to conduct X-ray velocimetry on a model that is physiologically realistic for an adult mammal.

METHOD

The experiments in this study were performed at the SPring-8 third generation synchrotron, Hyogo, Japan. The undulator beamline, 20XU (located within the medical imaging center), was used and the broadband synchrotron radiation was filtered by a Si-111 double crystal monochromator to provide a beam energy of 25 keV. A modified beam monitor (Hamamatsu AA50) was used to convert the X-rays into visible light using a 23 μm scintillator. The source to sample distance was 80 m and the optimal sample to detector distance was found to be 140 cm. A 10× objective lens (Nikon Brightfield CFI Plan Apo 10×/0.45) was coupled with the detector (Photron SA2 with 2 × 2 binning) to obtain the required effective pixel size of 1.8 μm^2. The spatial resolution of this system is designed to ensure accurate imaging of the silica microspheres, which have a mean diameter of 3.5 μm. The beam size at the sample was approximately 0.8 × 1.8 mm.

Geometric Parameters

Figure 1 shows the geometric parameters commonly used to define an idealized asymmetric stenosis: the major diameter D, the stenosed diameter d, the stenosis length L, and the eccentricity E. This study investigates a rigid stenosis with a reduction in area of 50% ($d/D = \sqrt{0.5}$), with an aspect ratio (L/D) of 2 and with one edge of the blood vessel remaining straight ($E/D = 0.25$). The profile used to define the stenosis geometry is a sinusoidal wave as described by
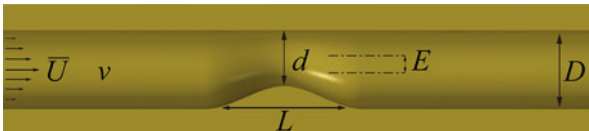

FIGURE 1. Geometric parameters used to define an asymmetric stenosis superimposed onto a cross-section of the CAD model used to create the *in vitro* model. $\overline{U}$ is the average velocity, v the kinematic viscosity, L and d the stenosis length and diameter, respectively, E the eccentricity, and D the vessel diameter.

Sheard *et al.*[40] The stenosis is modelled such that the cross-section remains circular throughout the length of the geometry. The model was manufactured by 3D-printing (Objet^{TM} FullCure$^®$ acrylic-based photopolymer), enabling geometries that standard machining techniques are not capable of producing. This high resolution technique, with a layer thickness of 16 μm ensured the model was accurate on the small scale being investigated. The major diameter D was chosen to be 1.5 mm to replicate a 3:1 femoral artery of a mouse, approximately 5 mm distal to the iliac bifurcation. The model has a lead-in section, both before and after the stenosis, of 10D in length. This ensures the flow is fully developed before the stenosis and that no sudden changes in geometry after the stenosis affect the resulting flow structures.

For pulsatile circulatory flow, two dimensionless parameters are typically used to characterize the flow: Reynolds number and Womersley number. The Reynolds number represents the ratio of inertial force to viscous force and is defined as

$$\text{Re} = \frac{UD}{v} , \qquad (2)$$

where U is the velocity and v is the kinematic viscosity (for this study whole blood is taken as $v = 2.83 \times 10^{-6} \, \text{m}^2 \, \text{s}^{-1}$). The Womersley number represents the ratio of unsteady force to viscous force, or the unsteady behavior of fluid flow in response to an oscillatory pressure gradient. The Womersley number is defined as

$$\alpha = \frac{D}{2}\sqrt{\frac{\omega}{v}} , \qquad (3)$$

where ω is the frequency of the pulsatile flow. The maximum Reynolds numbers measured in previous *in vivo* studies are provided in Table 1. The maximum Reynolds number is defined as

$$\text{Re}_{\text{max}} = \frac{U_{\text{max}}D^*}{v} , \qquad (4)$$

where U_{max} is the maximum velocity throughout the measurement and D^* is the diameter at which this velocity occurs. The majority of studies have investigated $\text{Re}_{\text{max}} \ll 1$, with only recent studies being capable of measuring *in vivo* flows at $\text{Re}_{\text{max}} \approx 1$. Additionally, the maximum vessel size previously investigated *in vivo* has been 250 μm due to the requirement of optical access. Previous X-ray velocimetry studies have investigated thicker samples *in vitro* than possible with optical PIV and are also shown in Table 1. Due to the relatively large exposure times required, all previous X-ray blood flow studies have had $\text{Re}_{\text{max}} < 1$. The current study investigates a

TABLE 1.   Maximum Reynolds number of previous *in vivo* optical PIV studies and *in vitro* X-ray velocimetry blood flow studies.

Year	Lead author	Subject	Vessels size (μm)	Max. velocity (mm s^{-1})	Re$_{max}$
Microscope techniques					
2002	Sugii[42]	Rat mesentery[a]	23.6	3.5	0.03
2003	Hove[18]	Zebrafish embryo heart[c]	14.5	5	0.03
2006	Vennemann[46]	Chicken embryo heart[b]	200	26	1.84
2009	Poelma[34]	Chicken embryo heart[b]	250	40	3.53
X-ray phase contrast imaging					
2005	Lee[28]	*In vitro*[d]	490	0.4	0.07
2006	Kim[21]	*In vitro*[d]	2770	0.5	0.49
2010	Irvine[20]	*In vitro*[e]	1900	1.1	0.74
2010	Dubsky[8]	*In vitro*[f]	707	0.05	0.01
	Current study	*In vitro*[d]	1060	22	8.24

[a] Standard, [b] Epifluorescent, [c] Confocal, [d] 2D, [e] Axisymmetric 3D, [f] CTXV 3D.
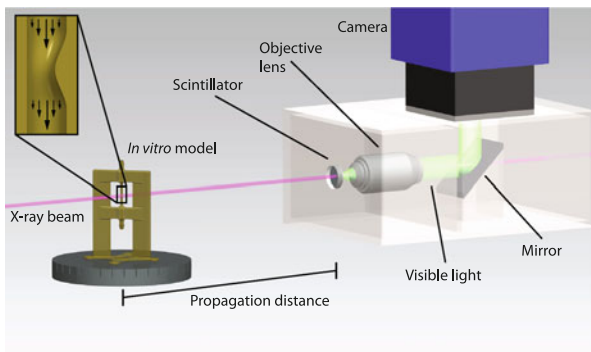

FIGURE 2.   Schematic setup of the micro X-ray velocimetry configuration. The X-ray beam (purple) penetrates the sample (stenosis model mounted on a CT stage) and interacts with the scintillator to produce visible light (green). An objective lens is used to magnify and focus the visible light from the scintillator onto the sensor of the camera. A mirror is used to remove the camera from the X-ray path. For reference, the X-ray beam size is 0.8 mm high × 1.8 mm wide.

significantly thicker section of whole blood than previously possible *in vivo* ($D = 1.5$ mm) with a maximum velocity of $U = 22$ mm s^{-1}, resulting in Re$_{max} = 8$, twice that of previous *in vivo* work and an order of magnitude greater than previous X-ray *in vitro* work.

X-ray PIV

X-ray velocimetry requires a pair of images of a seeded flow to be acquired at a specified time interval (ΔT). The images are divided into integration windows and cross correlation is utilized to determine the modal displacement of the particles; this combined with the known ΔT gives the instantaneous velocity. For more details of the specifics of the software analysis, the reader is referred to Fouras *et al.*[14]

The basic configuration required for X-ray velocimetry is shown in Fig. 2. The *in vitro* model is placed into the beam path such that the X-rays produced by the synchrotron penetrate the volume of flow being

investigated. The X-rays pass through the sample and strike a scintillator to produce visible light, enabling a standard scientific camera to be used; a mirror is placed in the optical path to ensure that the image sensor is not exposed to X-ray radiation. This setup produces volumetric data which, if under simple flow conditions, can be extracted to provide three-dimensional measurements.[12] The measurements in the current study are two-dimensional, with the cross-correlation providing the modal velocity, which, for parabolic like flows, can be assumed to be at the center of the model.

In Vitro Imaging

The experimental set-up consisted of an *in vitro* model, pump and flow probe connected in a closed loop system via silicone tubing. The working fluid was whole blood (rat blood purchased through SPring-8) seeded with 3.5 μm silica microspheres (Bangs Laboratories, Inc. SS05N/5903). The addition of microspheres allows the plasma velocity to be measured and increases the signal to noise ratio without adversely affecting the blood. A peristaltic pump (Walker P720/66) was used to circulate the blood through the system with a pulsatile flow. A flow probe (Transonic Systems Inc. TS410 transit-time tubing flowmeter with a 1PXN flow probe) was used to monitor the pulsatile blood flow of the system and a data acquisition module (IDT MotionPro) was used to record the data; the flow probe was situated upstream of the velocimetry measurement location. The frequency and flow rate of the pump were chosen to be highly pulsatile (3.3 Hz, $\alpha = 2.1$) and at a physiological flow rate for a mouse.

In order to achieve the temporal resolution required to measure *in vivo* flow rates, a high-speed camera was used (Photron Fastcam SA2, 1000 frames per second (fps) at full resolution of 4 MP). A region of interest was selected that corresponded to the location of the X-ray beam resulting in an image size of 1024 × 512 pixels.

The current study has made significant gains in the exposure times required to acquire synchrotron images for use in X-ray velocimetry, using exposure times of only 0.5 ms. The reduction in exposure time has been achieved through optimization of scintillator thickness, objective lens, and synchrotron settings. Previous studies have reported minimum exposures of 10–40 ms, with only two studies reporting exposures less than 10 ms.[8,20] This represents an increase of more than an order of magnitude in temporal resolution over the majority of previous studies and a sixfold improvement over the previous best. It is this decrease in exposure time that has been critical in the ability to measure at physiologically realistic flow rates. It should be noted that one study has reported structure-tracking velocimetry[48] with significantly lower exposure times; however, this technique utilizes double exposure images to achieve a small ΔT and can only acquire images at a rate of 1 Hz. This setup is not suitable for the current study as the analysis of double exposure images requires prior knowledge of the flow, and the temporal resolution is not high enough for a constantly changing system, such as *in vivo* blood flow.

An adverse result of high-speed imaging is the increased effect of high temporal frequency fluctuations in the X-ray beam, an effect not seen in experiments with longer exposures. These fluctuations are caused by instabilities in the electron beam orbit of the synchrotron which, coupled with the long distance

FIGURE 3. Comparison of left: raw and right: filtered images of whole blood seeded with $3.5\,\mu m$ silica microspheres. Inserts provide a magnified view of the same section. The filtered image has had spatial and temporal band-pass filters applied. The filtered image displays significantly improved signal to noise ratio and yields improved velocimetry measurements. For reference, the inset box is $90\,\mu m \times 90\,\mu m$.

between the source and the sample (80 m) and vibration of the monochromator, mean that the vertical position of the X-ray beam varies in time over the field of view.[30] This has a strong, negative effect on the capacity of PIV algorithms to accurately detect the motion of the tracer particles. This is overcome by post-processing the raw images using a spatial frequency filter to remove the low spatial frequency signal produced by the fluctuations in the X-ray beam. Additionally, since the depth of field in an X-ray image is effectively infinite, all material subjected to the X-ray beam appears in focus in the images, including the stationary structure of the model. This is removed by temporal band-pass filtering. Figure 3 shows a comparison of the raw image to the filtered one, illustrating the improvement in signal to noise ratio and a reduction in the spatial non-uniformity of the X-ray beam.

RESULTS

Multiple cycles of the periodic flow were acquired to enable phase averaging to be utilized, enhancing the precision of the velocity measurements. As the X-ray beam size limited the field of view, five positions were used to acquire data for both the converging and diverging sections of the model, and were then combined digitally. An overlap of 130 pixels between imaging locations was used to ensure that the velocity data could be tiled together. In total, 11 s of data (five acquisitions, each approximately seven cycles in length) were acquired over a 27 s time period, enabling confidence in the consistency of data at each position. The instantaneous vector field for each measurement location was calculated at a temporal resolution of 1 ms. The period (T) of the flow was determined by both the flow probe and the velocimetry to be 300 ms (3.3 Hz), corresponding to a heart rate of 200 beats per minute. The vectors were then phase averaged to create 16 bins in the 300 ms cycle, enough to accurately define the periodic wave used in this study, with a temporal measurement spacing of 18.9 ms.

Figure 4 shows the data acquired by the flow probe compared to the flow rate calculated from individual rows of the velocimetry measurements. The average flow rate is plotted along with the standard deviation. In order to estimate the flow rate from the 2D velocity measurements, axisymmetry was assumed and the velocity field was integrated over the cross-sectional area. This approach provides a quick and useful tool to establish confidence in the measurements. The peristaltic pump is shown to create two distinct pulses during each cycle, as does a beating heart, with significant gradients during the increase in flow rate of the first pulse and the decline in flow rate of the second
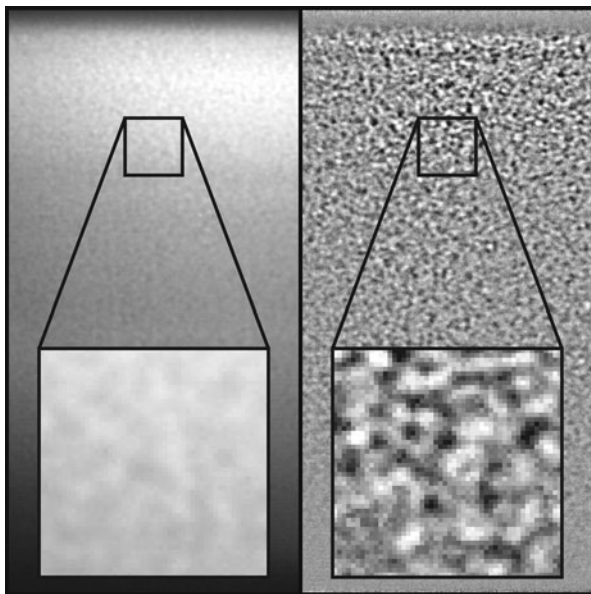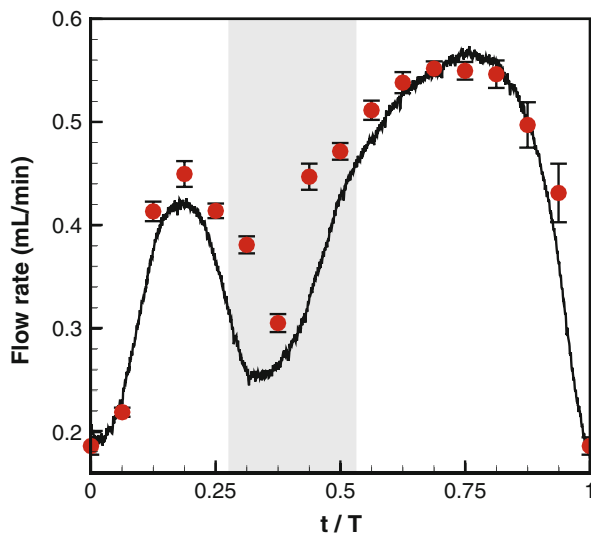
FIGURE 4. Flow rate measured by both the flow probe (solid line) and the velocimetry measurements (circle). Average flow is plotted over one period (300 ms) and error bars indicate one standard deviation from the mean. The gray area indicates the time points of measurements shown in Fig. 6.

pulse. There is good agreement between the measurement techniques over the entire cycle, with the velocimetry accurately measuring the minimum and maximum flow rate, frequency and clearly identifying temporal detail of both pulses. Additionally, the average flow rate measured by the flow probe was $0.399 \, \text{mL} \, \text{min}^{-1}$ compared to $0.418 \, \text{mL} \, \text{min}^{-1}$ as measured by velocimetry. This represents a 4.5% discrepancy between the techniques. Considering the flow probe is calibrated for whole blood, not blood seeded with silica microspheres, and given the assumption of axisymmetry, this process provides a good approximation of flow rate.

In order to combine the results acquired at multiple positions, each velocimetry vector field was vertically tiled together. WSS was calculated using the velocimetry measurements before tiling to ensure that the effects of tiling did not result in spurious WSS measurements. Velocity gradients were calculated using the method described in Fouras *et al.*[15] In this method accuracy of vorticity calculation has a second-order relationship with spatial sampling separation, thus a 50% reduction in velocity measurements results in a 75% reduction in the accuracy of the vorticity calculation. Figure 5 shows both the averaged vector field and the average WSS for the entire length of the stenosis. The interrogation windows used were 64×64 pixels with an overlap of 75%. For a detailed study of PIV parameters such as overlap the reader is referred to Theunissen *et al.*[44] The mean and maximal pixel displacements of particles were 5.1 and 12.3, respectively. Every fifth vector is shown in the vertical
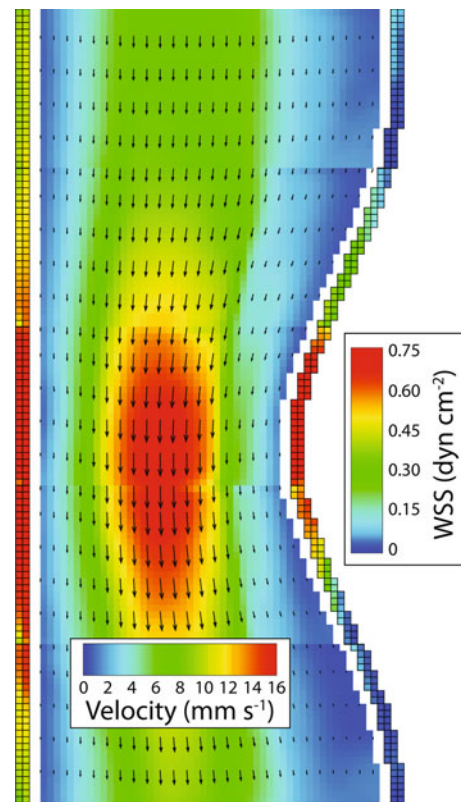

FIGURE 5. X-ray velocimetry measurements time averaged over the periodic cycle, with the corresponding average wall shear stress shown offset from the main geometry. Five measurement positions were acquired and are shown tiled vertically together. Vectors show the direction and magnitude of flow while overlaid contours show velocity magnitude. Vectors are calculated at 29 μm spacing. For clarity, only every fifth vector is shown in the vertical direction and every second in the horizontal direction. Contours bound by the black mesh and offset from the main geometry show the average wall shear stress over the periodic cycle. The mesh applied to the contours illustrates the resolution of the technique. Quantification of contours is provided within the figure.

direction and every second in the horizontal direction to help visualize the velocity profile between the stenosis walls. Flow is from the top of the page down and the contours show the velocity magnitude. The WSS is shown, offset from the flow field for clarity, with the mesh overlaid onto the contours illustrating the resolution of the measurement technique. The flow is seen to be parallel to the walls within the straight section of the model and increases in magnitude as the caliber of the model reduces, with the maximum velocity occurring in the center of the narrowest section. The horizontal component of velocity is seen to be greatest in the sections that exhibit greatest change in caliber. The flow is seen to be attached, as would be expected at this Reynolds number.[16] The WSS is seen to be low upstream of the stenosis, maximal at the throat and steadily reducing downstream of the throat. Additionally,

the downstream section of the non-stenosed wall displays higher WSS after the throat compared to the upstream section. This is thought to be due to RBCs taking longer to return to a uniform distribution across the cross-section of the diameter. This highlights the importance of using whole blood for *in vitro* experiments and the need for WSS to be calculated *in vivo*.

Figure 6 shows four time points of the phase averaged vector field for the entire length of the stenosis, starting from the sudden decrease in velocity at $\frac{5}{16}T$ (Fig. 4). This series was chosen to illustrate the capacity to temporally capture the pulsatile flow wave used in this study. As can be seen, the flow is initially at a mid-range velocity (a), drops to a low velocity (b), sharply increases to a high velocity (c), which then continues to rise gradually (d). While Fig. 4 illustrates the global features of the flow, Fig. 6 is able to display the local variations within the flow field.

The WSS can be displayed both temporally and spatially as surface plots, over the entire periodic cycle, as shown in Fig. 7, for both the straight and stenosed walls, allowing areas of high and low WSS to be clearly identified. The location on the wall at which the WSS is calculated is given as a ratio of its distance from the throat of the stenosis. The WSS is seen to be highest during the latter part of the periodic cycle, when the flow rate is the highest, at the throat of the stenosis, with both walls experiencing a similar amount of stress.

This information can be interpreted more easily by plotting in just one dimension; time or space. Figure 8 shows the WSS at $\frac{6}{16}T$ (Fig. 6b) for both the straight and stenosed walls. Artifacts of the tiling can be seen; however, these do not restrict interpretation of the data. Figure 8 shows the similarity of WSS between the straight and stenosed walls at the throat of the stenosis. In contrast, Fig. 8 also shows the large
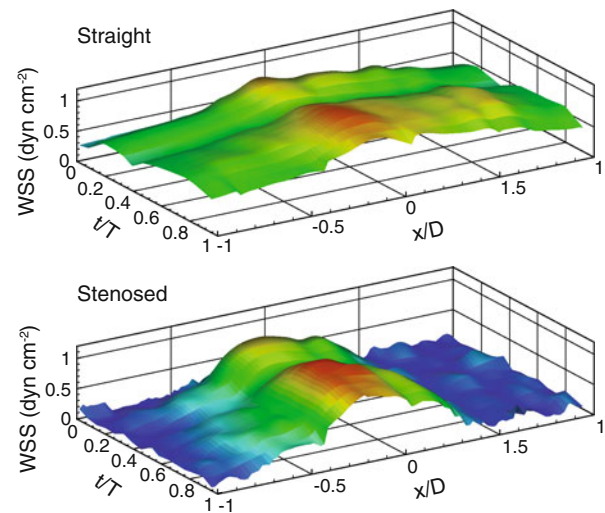
FIGURE 7. Wall shear stress for both the straight and stenosed walls. Surface displays the WSS in terms of location with regards to the stenosis throat and phase within the pulsatile cycle. For clarity contours also show WSS.
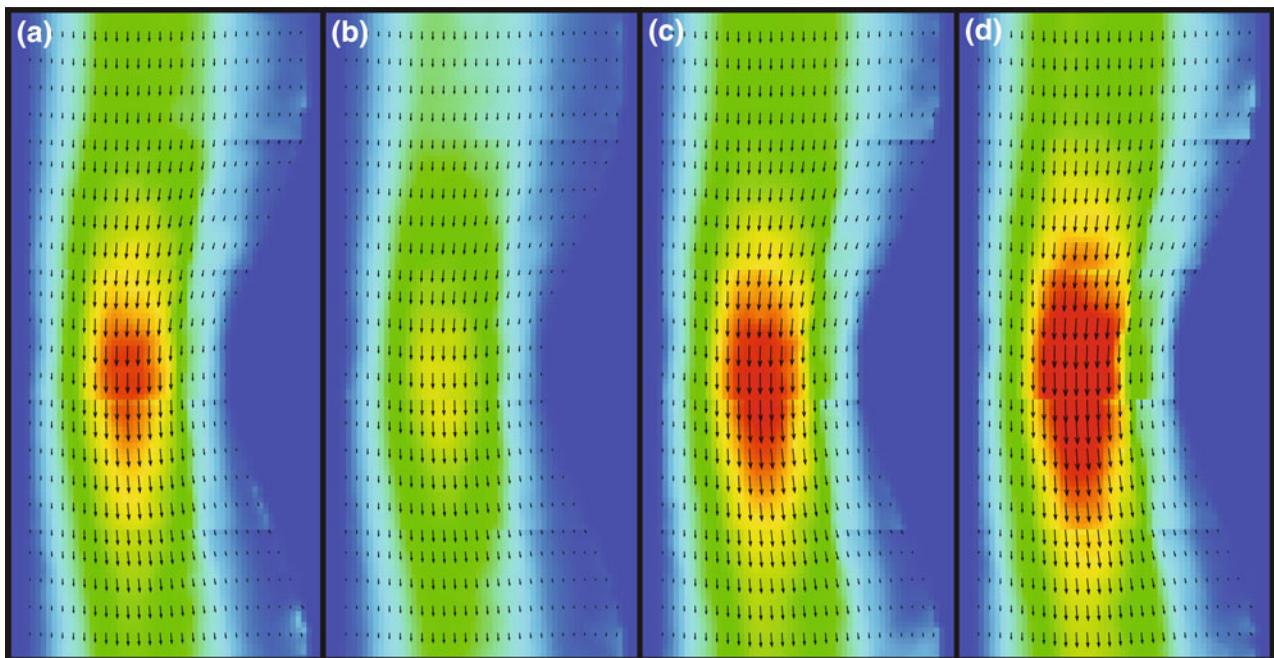
FIGURE 6. X-ray velocimetry measurements at (a) $\frac{5}{16}T$, (b) $\frac{6}{16}T$, (c) $\frac{7}{16}T$, and (d) $\frac{8}{16}T$, as indicated in Fig. 4. Five measurement positions were acquired for each time bin and are shown tiled vertically together. Measurements are phase averaged and show the direction and magnitude of flow while contours show the velocity magnitude (contour levels are consistent with Fig. 5).
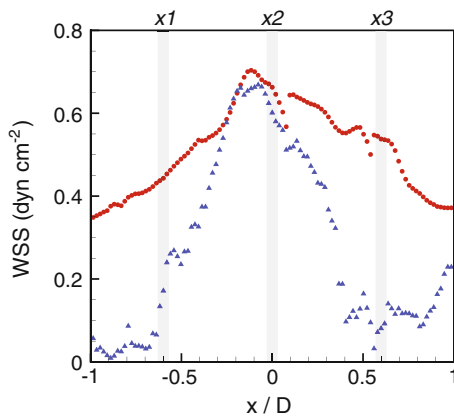
FIGURE 8. Wall shear stress measurements for one time bin in the periodic cycle ($\frac{6}{16}T$, velocity map also shown in Fig. 6b. Data for both the straight (circle) and stenosed (triangle) walls are shown. The shaded areas indicate the position of measurements given in Fig. 9.

variation between the straight and stenosed walls WSS both upstream and downstream of the throat. The lowest WSS is experienced at the upstream and downstream ends of the stenosed wall. Furthermore, this figure in conjunction with Fig. 7 shows that the WSS at the straight wall is always higher than that at the stenosed wall. This observation implies that once a vessel is stenosed, it is most likely that future plaques will occur on the stenosed side of the blood vessel, increasing its length rather than continuing to develop around the diameter of the vessel. The maximum WSS on the stenosed wall is located just upstream of the throat, indicating that this location is at highest risk of plaque rupture, leading to platelet activation, clotting, and possible infarction.

Figure 9 shows the WSS for three positions, as indicated in Fig. 8, over the periodic cycle for both the straight and stenosed walls ($x/D = -0.6$, $x/D = 0$, and $x/D = 0.6$). It can be seen that upstream of the throat of the stenosis ($x1$), there is a consistent difference in WSS over the entire cycle, with the stenosed wall constantly experiencing a lower WSS. Additionally, the influence of the periodic cycle can be seen, with both peaks clearly identifiable. At the throat of the stenosis ($x2$), both the straight and stenosed walls experience a similar WSS over the entire cycle, once again the influence of the periodic cycle is clear. However, inspection of the location downstream of the throat ($x3$) gives an interesting result. Although the WSS at the straight wall is seen to return to a similar shape to that upstream, the downstream wall is shown to flatten out and display little influence from the periodic flow. Additionally, the WSS of the straight wall downstream ($x3$) is consistently higher than upstream ($x3$), whereas the opposite is true for the stenosed wall. It is in this location, downstream on the
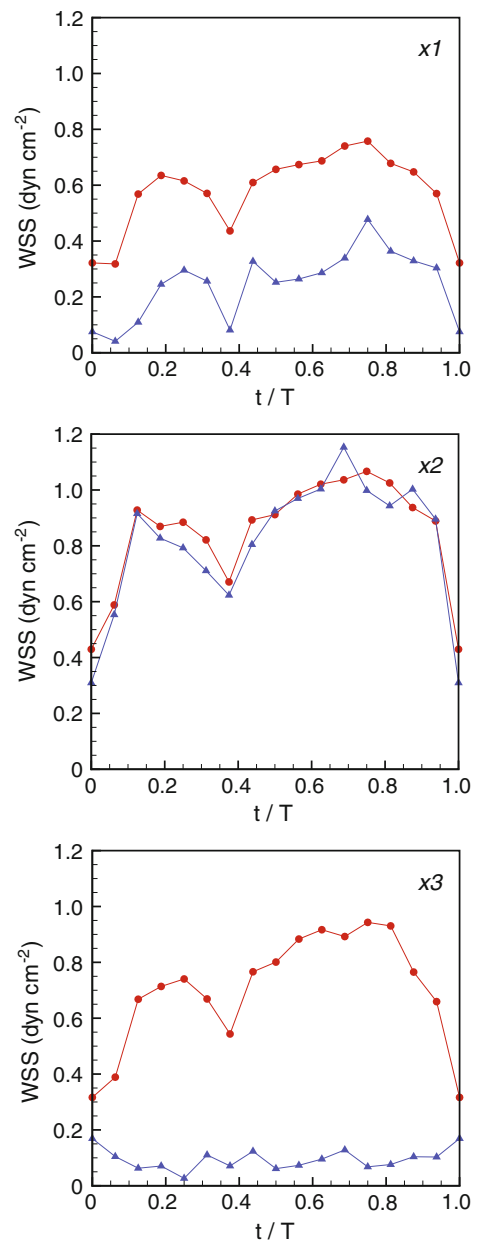

FIGURE 9. Wall shear stress measurements for three positions in the stenosis; $x1$ 0.6D upstream of the throat, $x2$ at the throat, and $x3$ 0.6D downstream of the throat. Data for both the straight (cirlce) and stenosed (triangle) walls are shown.

stenosed wall, that recirculation zones are seen to occur at higher Reynolds numbers.[16]

CONSIDERATIONS FOR *IN VIVO* MEASUREMENT

In order for this technique to transition from *in vitro* to *in vivo* velocity and WSS measurements several points first need to be addressed. As synchrotron X-ray

PCI captures information relating to all tissue that the X-ray beam passes through, *in vivo* images will contain unwanted artifacts from surrounding tissue, bones and airways. However, the majority of these unwanted artifacts can be remove using the filtering processes described in this study. The use of tracer particles in this study to increase the signal to noise ratio to levels surpassing those required *in vitro* has helped develop the current technique towards the capability for *in vivo* measurements. Calculation of wall shear stress will be more difficult *in vivo* as vessel walls may move due to blood flow, breathing and cardiac movement. However, this difficulty is present in all *in vivo* techniques and has been successfully overcome in previous optical PIV studies.[42] The authors feel that future studies will also be able to overcome these difficulties with X-ray velocimetry by appropriate tracer particles and PIV algorithms allowing dynamic boundaries.

Additionally, in order to measure greater velocities, exposure times need to be reduced. A decrease in exposures of an order of magnitude would allow for the investigation of even larger vessels. This represents only a small improvement when compared to the improvements presented in this paper. The beamline that this study was conducted on utilizes a monochromator that removes 99.99% of the available light. Moving to a beamline utilising a larger fraction of available light would result in significantly lower exposure times, and has been shown to still be suitable for velocimetry measurements of blood flows.[21]

CONCLUSION

This study has demonstrated the ability of X-ray velocimetry to image pulsatile blood flow in an *in vitro* model at a physiologically realistic flow rate. A highly pulsatile flow ($0.42 \, \text{mL min}^{-1}$, 200 bpm) was accurately measured at high temporal and spatial resolution (1 ms and 29 μm vector spacing). Two-dimensional velocity measurements were successfully converted to flow rate measurements by assuming axisymmetry. A flow probe was used to independently confirm the flow rate measured by velocimetry with a discrepancy of 4.5% between measurement techniques. Additionally, the flow probe and velocimetry agreed strongly with the maximum and minimum flow rates and the frequency of the flow. The wall shear stress was calculated from the velocity flow field at high enough resolution to clearly identify local variations. Furthermore, it showed features that would be expected within this geometry at the flow rate investigated. These results confirm X-ray velocimetry as a suitable technique for *in vivo* studies of haemodynamics with highly pulsatile flow in fully developed mammalian models, provided

the appropriate signal to noise ratio can be maintained. The ability to perform velocimetry *in vivo* will lead to high resolution velocity measurements and result in highly accurate wall shear stress measurements, critical for developing our understanding of the effect of haemodynamics on arterial disease.

REFERENCES

[1]Adrian, R. J. Particle-imaging techniques for experimental fluid-Mechanics. *Annu. Rev. Fluid Mech.* 23:261–304, 1991.
[2]Augst, A. D., D. C. Barratt, A. D. Hughes, F. P. Glor, S. A. M. Thom and X. Y. Xu. Accuracy and reproducibility of CFD predicted wall shear stress using 3D ultrasound images. *J. Biomech. Eng. Trans.* ASME 125:218–222, 2003.
[3]Baek H., M. V. Jayaraman, and G. E. Karniadakis. Wall shear stress and pressure distribution on aneurysms and infundibulae in the posterior communicating artery bifurcation. *Ann. Biomed. Eng.* 37(12):2469–2487, 2009.
[4]Benveniste, H., and S. Blackband. MR microscopy and high resolution small animal MRI: applications in neuroscience research. *Prog. Neurobiol.* 67:393–420, 2002.
[5]Cheng, C., D. Tempel, R. van Haperen, A. van der Bann, F. Grosveld, M. J. A. P. Daemen, R. Krams, and R. de Crom. Atherosclerotic lesion size and vulnerability are determined by patterns of fluid shear stress. *Circulation* 113:2744–2753, 2006.
[6]Chytilova, E., J. Malik, Z. Kasalova, R. Dolezalova, T. Stulc, and R. Ceska. Lower wall shear rate of the common carotid artery in treated type 2 diabetes mellitus with metabolic syndrome. *Physiol. Res.* 58:185–191, 2009.
[7]Davis, T. J., D. Gao, T. E. Gureyev, A. W. Stevenson, and S. W. Wilkins. Phase-contrast imaging of weakly absorbing materials using hard X-rays. *Nature* 373:595–598, 1995.
[8]Dubsky, S., R. A. Jamison, S. C. Irvine, K. K. W. Siu, K. Hourigan, and A. Fouras. Computed tomographic X-ray velocimetry. *Appl. Phys. Lett.* 96:023702, 2010.
[9]Dubsky, S., R. A. Jamison, S. P. A. Higgins, K. K. W. Siu, K. Hourigan, and A. Fouras. Computed tomographic X-ray velocimetry for simultaneous 3D measurement of velocity and geometry in opaque vessels. *Exp. Fluids*, 2010. doi:10.1007/s00348-010-1006-x.
[10]Ford, M. D., H. N. Nikolov, J. S. Milner, S. P. Lownie, E. M. Demont, W. Kalata, F. Loth, D. W. Holdsworth, and D. A. Steinman. PIV-measured versus CFD-predicted flow dynamics in anatomically realistic cerebral aneurysm models. *J. Biomech. Eng. Trans.* ASME 130(2):021015, 2008.

[11]Forouhar, A. S., M. Liebling, A. Hickerson, A. Nasiraei-Moghaddam, H. Tsai, J. R. Hove, S. E. Fraser, M. E. Dickinson, and M. Gharib. The embryonic vertebrate heart tube is a dynamic suction pump. *Science* 312:751–753, 2006.

[12]Fouras, A., J. Dusting, R. Lewis, and K. Hourigan. Three-dimensional synchrotron X-ray particle image velocimetry. *J. Appl. Phys.* 102:064916, 2007.

[13]Fouras, A., M. J. Kitchen, S. Dubsky, R. A. Lewis, S. B. Hooper, and K. Hourigan. The past, present, and future of X-ray technology for *in vivo* imaging of function and form. *J. Appl. Phys.* 105:102009, 2009.

[14]Fouras, A., D. Lo Jacono, and K. Hourigan. Target-free stereo PIV: a novel technique with inherent error estimation and improved accuracy. *Exp. Fluids* 44(2):317–329, 2008.

[15]Fouras, A., and J. Soria. Accuracy of out-of-plane vorticity measurements derived from in-plane velocity field data. *Exp. Fluids* 25:409–430, 1998.

[16]Griffith, M. D., T. Leweke, M. C. Thompson, and K. Hourigan. Pulsatile flow in stenotic geometries: flow behaviour and stability. *J. Fluid Mech.* 622:291–320, 2009.

[17]Hoi, Y., S. H. Woodward, M. Kim, D. B. Taulbee, and H. Meng. Validation of CFD simulations of cerebral aneurysms with implication of geometric variations. *J. Biomech. Eng. Trans. ASME* 128:844–851, 2006.

[18]Hove, J. R., R. W. Koster, A. S. Forouhar, G. Acevedo-Bolton, S. E. Fraser, and M. Gharib. Intracardiac fluid forces are an essential epigenetic factor for embryonic cardiogenesis. *Nature* 421:172–177, 2003.

[19]Irvine, S. C., D. M. Paganin, S. Dubsky, R. A. Lewis, and A. Fouras. Phase retrieval for improved three-dimensional velocimetry of dynamic X-ray blood speckle. *Appl. Phys. Lett.* 93:153901, 2008.

[20]Irvine, S. C., D. M. Paganin, A. Jamison, S. Dubsky, and A. Fouras. Vector tomographic X-ray phase contrast velocimetry utilizing dynamic blood speckle. *Opt. Exp.* 18:2368–2379, 2010.

[21]Kim, G. B., and S. J. Lee. X-ray PIV measurements of blood flows without tracer particles. *Exp. Fluids* 41:195–200, 2006.

[22]Kim, G. B, N. Y. Lim, and S. J. Lee. Hollow microcapsules for sensing micro-scale flow motion in X-ray imaging method. *Microfluid. Nanofluid.* 6:419–424, 2009.

[23]Kim, M., D. B. Taulbee, M. Tremmel, and H. Meng. Comparison of two stents in modifying cerebral aneurysm hemodynamics. *Ann. Biomed. Eng.* 36(5):726–741, 2008.

[24]Ku, J. P., M. T. Draney, F. R. Arko, A. Lee, F. P. Chan, N. Pelc, C. K. Zarins, and C. A. Taylor. *In vivo* validation of numerical prediction of blood flow in arterial bypass grafts. *Ann. Biomed. Eng.* 30:743–752, 2002.

[25]Lee, J. Y., H. S. Ji, and S. J. Lee. Micro-PIV measurements of blood flow in extraembryonic blood vessels of chicken embryos. *Physiol. Meas.* 28:1149–1162, 2007.

[26]Lee, S. J., S. Y. Jung, and S. Ahn. Flow tracing microparticle sensors designed for enhanced X-ray contrast. *Biosens. Bioelectron.* 25:1571–1578, 2010.

[27]Lee, S. J., and G. B. Kim. X-ray particle image velocimetry for measuring quantitative flow information inside opaque objects. *J. Appl. Phys.* 94:3620–3623, 2003.

[28]Lee, S. J., and G. B. Kim. Synchrotron microimaging technique for measuring the velocity fields of real blood flows. *J. Appl. Phys.* 97:064701, 2005.

[29]Li, M. X., J. J. Beech-Brandt, L. R. John, P. R. Hoskins, and W. J. Easso. Numerical analysis of pulsatile blood flow and vessel wall mechanics in different degrees of stenoses. *J. Biomech.* 40:3715–3724, 2007.

[30]Morgan, K. S., S. C. Irvine, Y. Suzuki, K. Uesugi, A. Takeuchi, D. M. Paganin, and K. K. W. Siu. Measurement of hard X-ray coherence in the presence of a rotating random-phase-screen diffuser. *Opt. Commun.* 283:216–225, 2010.

[31]Mouse Genome Sequencing Consortium. Initial sequencing and comparative analysis of the mouse genome. *Nature* 420:520–562, 2002.

[32]Moyle, K. R., L. Antiga, and D. A. Steinman. Inlet conditions for image-based CFD models of the carotid bifurcation: Is it reasonable to assume fully developed flow? *J. Biomech. Eng. Trans. ASME* 128:371–379, 2006.

[33]Nesbitt, W. S., E. Westein, F. J. Tovar-Lopez, E. Tolouei, A. Mitchell, J. Fu, J. Carberry, A. Fouras, and S. P. Jackson. A shear gradient-dependent platelet aggregation mechanism drives thrombus formation. *Nat. Med.* 15:665–673, 2009.

[34]Poelma, C., V. Heiden, B. P. Hiereck, R. E. Poelmann, and J. Westerweel. Measurements of the wall shear stress distribution in the outflow tract of an embryonic chicken heart. *J. R. Soc. Interface* 7:91–103, 2010.

[35]Poelma, C., J. M. Mari, N. Foin, M. X. Tang, R. Krams, C. G. Caro, P. D. Weinberg, and J. Westerweel. 3D Flow reconstruction using ultrasound PIV. *Exp. Fluids*, 2009. doi:10.1007/s00348-009-0781-8.

[36]Poelma, C., P. Vennemann, R. Lindken, and J. Westerweel. *In vivo* blood flow and wall shear stress measurements in the vitelline network. *Exp. Fluids* 45:703–713, 2008.

[37]Reneman, R. S., T. Arts, and A. P. G. Hoeks. Wall shear stress–an important determinant of endothelial cell function and structure—in the arterial system *in vivo*. *J. Vasc. Res.* 43:251–269, 2006.

[38]Rosencranz, R., and S. A. Bogen. Clinical laboratory measurement of serum, plasma, and blood viscosity. *Pathol. Patterns Rev.* 125:S78–S86, 2006.

[39]Ross R. Cell biology of atherosclerosis. *Annu. Rev. Physiol.* 57:791–804, 1995.

[40]Sheard, G. J. Flow dynamics and wall shear-stress variation in a fusiform aneurysm. *J. Eng. Math.* 64:379–390, 2009.

[41]Smith, M. L., D. S. Long, E. R. Damiano, and K. Ley. Near-wall μ-PIV reveals a hydrodynamically relevant endothelial surface layer in venules *in vivo*. *Biophys. J.* 85:637–645, 2003.

[42]Sugii, Y., S. Nishio, and K. Okamoto. *In vivo* PIV measurement of red blood cell velocity field in microvessels considering mesentery motion. *Physiol. Meas.* 23:403–416, 2002.

[43]Texon M. Hemodynamic concept of atherosclerosis. *Am. J. Cardiol.* 5:291–294, 1960.

[44]Theunissen, R., F. Scarano, and M. L. Riethmuller. Spatially adaptive PIV interrogation based on data ensemble. *Exp. Fluids* 48:875–887, 2010.

[45]Thomas S. M. The current role of catheter angiography. *Imaging* 13:366–375, 2001.

[46]Vennemann, P., K. T. Kiger, R. Lindken, B. C. Groenendijk, S. Stekelenburg-de Vos, T. L. ten Hagen, N. T. Ursem, R. E. Poelmann, J. Westerweel, and B. P. Hierck. *In vivo* micro particle image velocimetry measurements of blood-plasma in the embryonic avian heart. *J. Biomech.* 39:1191–1200, 2006.

[47]Vennemann, P., R. Lindken, and J. Westerweel. *In vivo* whole-field blood velocity measurement techniques. *Exp. Fluids* 42:495–511, 2007.

[48]Wang, Y., X. Liu, K. Im, W. Lee, J. Wang, K. Fezzaa, D. L. S. Hung, and J. R. Winkelman. Ultrafast X-ray study of dense-liquid-jet flow dynamics using structure-tracking velocimetry. *Nat. Phys.* 4:305–309, 2008.

[49]Wen, C. Y., A. S. Yang, L. Y. Tseng, and J. W. Chai. Investigation of pulsatile flowfield in healthy thoracic aorta models. *Ann. Biomed. Eng.* 38(2):391–402, 2010.